TITLE: A Fundamental Study of Charge Effects on the Melt Electrowritten Polymer Fibers

Authors: Houzhu Ding, Kai Cao, Fucheng Zhang, William Boettcher, Robert C. Chang *

Affiliations: Department of Mechanical Engineering, Stevens Institute of Technology, Hoboken, NJ, 07030, USA

*** Name and address for correspondence:** Dr. Robert C. Chang, 1 Castle Point Hudson, Hoboken, NJ 07030. Email: rchang6@stevens.edu. Tel.: 201-216-8301

Abstract:

Melt electrowriting (MEW) is an electrohydrodynamics (EHD)-based additive manufacturing paradigm for printing microscale fibers. Although models for charge transport during EHD printing have been described, significant challenges arise from the in-process charge dynamics in MEW process, which limits the achievable print resolution. This paper advances a methodology to analyze the effects of charge dynamics on the MEW-printed structure resolution. First, fibers printed with an oscillating toolpath exhibit two distinct alignment patterns with constituent fibers either successively overlapping along the toolpath or diverging into individual fibers without apparent overlap on conductive and non-conductive substrates, respectively, pointing to the existence of inter-fiber charge phenomena. Next, a set of straight fibers are printed on two types of substrates to investigate the relationship between the prescribed inter-fiber distance (set S_f) and measured S_f. Both repulsion (measured $S_f >$ set S_f) and attraction (measured $S_f <$ set S_f) are observed. Moreover, a mathematical model based on line-point charge interactions is advanced to explain the fiber attraction-repulsion phenomenon. Finally, residual charge measurements with a customized Faraday Cup reveal that printed scaffolds on conductive and non-conductive substrates are negatively and positively charged for residual charge, respectively.

Keywords: Melt electrowriting; Residual charge; Substrate conductivity

1. Introduction

Additive manufacturing (AM) processes enable the fabrication of complex structures for engineered tissue applications [1–4]. Among the established AM techniques, melt electrowriting (MEW) based on the electrohydrodynamical (EHD) phenomenon [5–7], is a prevailing technique to fabricate fibers at the micron to sub-micron scale. MEW has shown biological applications due to its solvent-free processing characteristics compared to its solution counterpart [8–10]. The 3D biomaterial-based porous constructs produced in this way, termed scaffolds, are mainly used as engineered tissue models, typified by ordered porous microarchitecture [11–13]. The two key measurement outcomes of the fabricated MEW structures are tailored fiber diameter and alignment of fibers. Recently, significant efforts have been made in terms of the process optimization to achieve a uniform fiber diameter by altering the key parameters such as applied voltage, polymer temperature, volumetric flow rate, and the tip-to-collector distance [6,14–16]. Traditionally, the second feature relating to the tight control over the orderly alignment of fibers and layers, is a comparatively neglected research direction, which is commonly believed to be dependent more on electro-mechanical process control. However, as in other EHD produced outcomes, the residual charge acquired by MEW fibers has been shown to cause intra-process jet instabilities, directly affecting the deposition accuracy. Therefore, the achievable inter-fiber distance is limited. The observed repulsion between adjacent printed fibers has been reported, whereby the residual charge is presumed to affect the electric field when the structural print reaches a prescribed number of layered fibers [17]. However, fundamental mechanism of how the charge can affect the printed fiber is still challenging in MEW process although the charge transport mechanism is well-established for a solution electrospinning process [18–20]. During the solution electrospinning process, the positive charges are transferred from the nozzle to the solution. Before the jet impacts the collector plates, charges can be dissipated through coronal discharge, solution vaporization and charge removal by humidity [18]. Upon deposition, partial charges, termed residual charges, are retained in the deposited fibers since the electrospun fibers are essentially electrets, a dielectric material capable of retaining charges at steady state [21]. Other charges are transferred to the collector substrate and flow to the negative electrode of the high voltage source. The residual charges have been shown to cause the instability of printing fibers, resulting in a conical accumulation shape on a stationary collector. Specifically, when a lateral perturbation grows in response to the repulsive forces between adjacent elements of charge carried by the fiber, the motion of the jet segments rapidly evolves into an electrically-driven bending instability [20,22,23].

However, the mechanism of how charge affects the jet instability explains more of the underlying physics when the fiber are "in-flight" rather than deposited well-aligned fibers. Such explanations are not applicable to the current MEW process under study. Specifically, the fundamental issue that occurs in MEW is stated as follows: When printing at a close inter-fiber distance, a minimum ratio of inter-fiber distance to fiber diameter (S_f/d_f) is determined to be 12, below which the adjacent fibers will either fuse into a single fiber or undergo repulsion [6]. Evidence points to the fact that the residual charge is one of the critical barriers to achieve precise fiber placement towards a highly ordered 3D mesh structure. However, there exists limited literature that quantitatively describes the charge transport phenomena between the deposited fiber and collector substrate, along with the effect of residual charge on the ratio of the inter-fiber distance to the fiber diameter. Furthermore, there have been few reported measurements of the residual charge due to its nanoscale magnitude [19,24].

To fill these knowledge gaps in printing uniform and highly ordered microstructures, a systematic, mechanistic study is advanced herein to explore the effects of charge on printed fiber outcomes by way of quantitative measurements and a preliminary mathematical model. Based on the experiments conducted on different conductive coverslips as substrates investigation of the charge effect on fiber alignment, this paper aims to provide needed insights into how residual charge compromises tight control over the orderly alignment of fibers under the emerging MEW paradigm to produce engineered scaffolds with precise control over structural properties.

2. Materials and Methods

2.1. Material and system configuration

Poly(ε-Caprolactone) (PCL) polymer in pellet form is selected for the MEW process with an average molecular weight of 45,600 g/mol and polydispersity of 1.219 (Capa6500, Perstop Ltd. of UK). The MEW system applied in this paper is schematized in Figure 1. PCL melt is loaded in a glass Luer-lock 5 mL syringe (Hamilton, USA),which is extruded by a

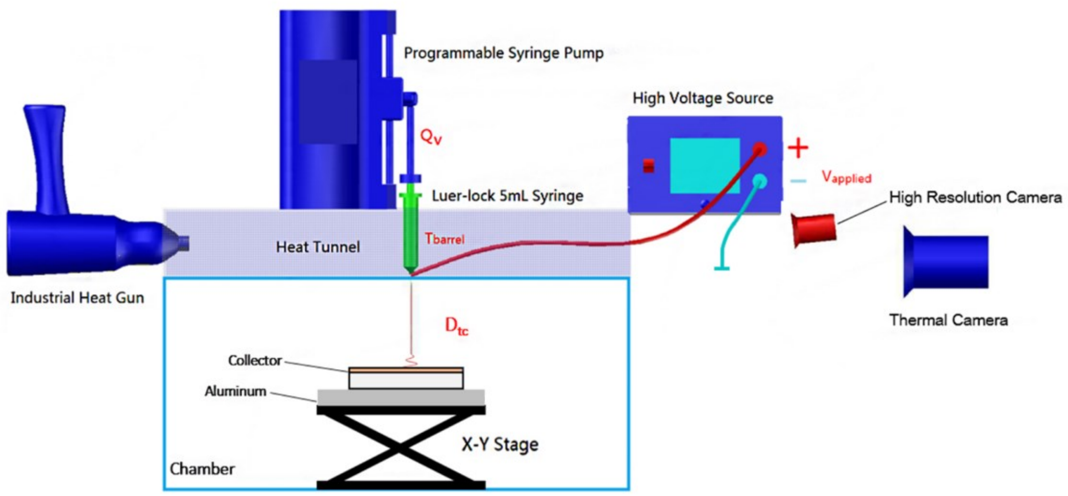

Figure 1. The MEW system configuration and details of the collector design

programmable syringe pump (Harvard Apparatus, USA) at a volumetric flow rate (Q_v) of 25 μL/h for all the experiments. The syringe barrel is heated by the industrial heat gun (Steinel, HG 2510 ESD, DE) set at 170 °C along the heat tunnel and the underside of the heat tunnel is penetrated by the nozzle, surrounded by thermal insulation tape. The length of the exposed nozzle is around 2 mm. An approximate voltage of 10 kV is applied between the nozzle tip and a grounded copper collector plate by a high voltage source (Gamma, USA). An X-Y stage (ASI Inc., USA) and the collector plate are sequentially mounted on a lab jack (Newport 281, USA). The distance between the nozzle tip and the collector plate (D_{tc}) is 12 mm. The temperature at the base of the syringe barrel is monitored with a FLIR thermometer (Cole-Parmer, USA) and kept at 59.5±1 °C. The ambient temperature and relative humidity is monitored with a multimeter (Extech Instruments, USA). Two types of fiber collecting surfaces are used in the experiments, namely an indium tin oxide (ITO) coated conductive substrates (SPI supplies, USA) with a resistivity range of 70-100 ohms and dimensions of 70×50 mm and a non-conductive polystyrene (PS) substrates (Fisherbrand, USA) with dimensions of 70×50 mm. PS refers to the non-conductive substrate all experiments unless stated otherwise. Table 1 lists the typical parameters and their range of values for the MEW process. In this paper, the conductivity of collection substrates and the user input S_f (set S_f), along with the process voltage and temperature are key parameters investigated.

2.3. Imaging and data analysis

An inverted motorized microscope (IX83, Olympus, USA) along with its imaging processing software (CellSens 2.11) is used to image and characterize all samples. A 20× objective lens with a magnification set at 12.6 is adopted for all samples. A 1080P,60 fps, industry microscope camera with 0.5× to 4.5× objective (Lapsun, CN) is used to take high resolution images and video of the printing process.

Table 1. The MEW process parameters and experimental values.

Parameters	Values
Polymer temperature (T_p)	59.5±1 °C (measured)
Applied Voltage (V)	10 kV
Stage translational speed (v_s)	1~50 mm/s
Volumetric flow rate (Q_v)	25 µL/h
Tip to collector distance (D_{tc})	12 mm
Inter-fiber distance (S_f)	0-1500 µm
Set temperature range (T_s)	170 °C

3. Results

3.1. Effect of substrate conductivity on fiber alignment

During the MEW process, key parameters including voltage V, temperature T_p, volumetric flow rate Q_v, and tip-to-collector distance D_{tc} have been previously identified

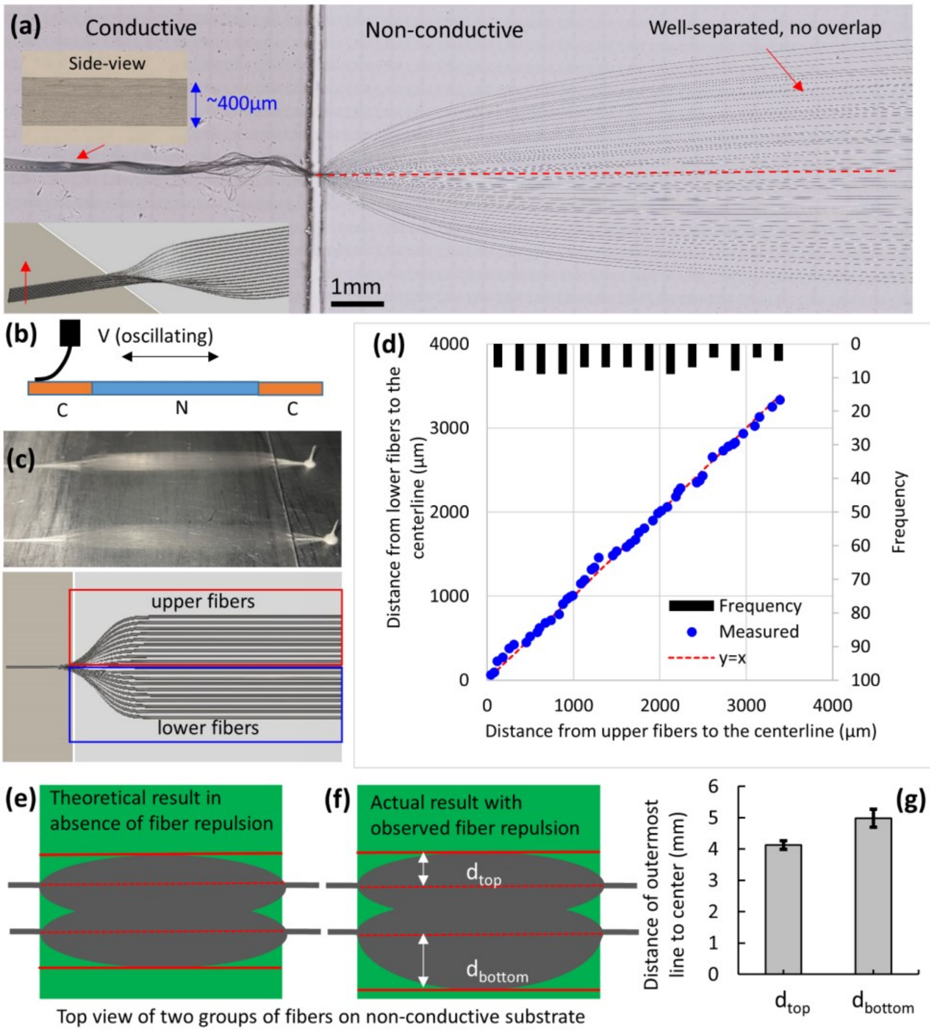

Figure 2. The printed fiber alignment patterns observed on two substrates with variable electric conductivities that are mounted in series on a moveable collecting stage: **(a)** Fibers precisely overlap on the conductive substrate and diverge into individual fibers on the non-conductive substrate; Lower left inset: color image of two groups of printed fibers (100 fibers each) **(b)** Schematic of printing configuration depicting the stage oscillating along a single toolpath; **(c)** Number of upper fibers and lower fibers are symmetric relative to the centerline prescribed by toolpath; **(d)** Symmetric plot of the distance from the upper and lower fibers to the central line along with their frequency. **(e)-(g)** Schematic illustrating the disposition for two groups of fibers printed for a theoretical case where no fiber repulsion compared to the actual result observed showing that the successively deposited fibers on non-conductive fibers are repulsed downwards.

[15,25–27]. However, the residual charge on fibers are demonstrated to have a significant effect on the inter-fiber spacing between aligned fiber prints. In this section, a set of qualitative experiments are designed to reveal the effect of substrate conductivities on the fiber alignment geometry. First, the key parameters required for stable jet formation are prescribed at: V=10kV, Q_v=25μL/h, T_p=58.5°C, D_{tc}=12mm. Two coverslip substrates with different conductivities are mounted in series on a translating stage to collect the printed fibers. The stage oscillates along the prescribed toolpath at a speed of 35mm/s. As a demonstration, 50 cycles of fibers are printed along a lateral center line distance of 35 mm that is coincident with the prescribed toolpath. According to Figure 2(a), distinct fiber alignment patterns are observed for the fiber deposition onto the left conductive substrate compared to the right non-conductive substrate. Specifically, 100 printed fibers are shown to precisely overlap on the conductive substrate and diverge into distinct individual fibers on the non-conductive substrate. In Figure 2(b), a schematic of the printing configuration is shown, in which the translating stage oscillates back and forth between the aligned substrates. As a result, the upper image in Figure 2(c) shows the color image of two groups of printed fibers, where the upper and bottom fibers are symmetrically distributed. To confirm that the newly deposited fibers are repulsed by previous fibers, a measurement of distance from upper and lower fibers to the center line coinciding with the prescribed toolpath, along with their frequency are plotted in Figure 2(d). Based on an individual fiber count, an approximately equal number of diverging fibers are deposited on each side of the centerline (i.e. 49 and 51 for upper and lower fibers, respectively). Each fiber is numbered (indexed from 1 to 49 for upper fibers and 1 to 51 for lower fibers) based on increasing distance from the center line. The distance of the upper fiber and lower fiber with the same index establishes the x and y coordinate values of the corresponding point in Figure 2(d), respectively. The obtained points are observed to be closely distributed along the line y = x. Additionally, considering the frequency distribution, it is clearly shown that upper fibers and lower fibers are not only symmetrical but also evenly distributed with respect to the center line. To further validate the fiber repulsion phenomenon, Figure 2 (e)-(g) show the schematic of two groups of fibers printed with a 35mm centerline distance. The d_{top} and d_{bottom} represent the distance between uppermost and bottommost fibers to the center line, respectively. Actual measurement result shows the later deposited fibers (bottom group) on non-conductive fibers are repulsed downwards overall, which results in $d_{bottom}>d_{top}$.

3.2. Effect of substrate conductivity on inter-fiber distance (S_f)

According to the results shown in section 3.1, fiber spacing or alignment mechanism are affected greatly by substrate conductivity. This section aims to investigate quantitative relationship between user set S_f and measured S_f. Experimentally, the deposition of two fibers cannot be positionally controlled when the set S_f is smaller than $8d_f$ [6]. Empirically, the fiber entrapped charges are considered as the contributing factor to this fiber positional constraint. In this section, a set of parallel fibers are printed on two types of substrates with different conductivities. It is assumed that the conductive coverslip serves as a fiber substrate to promote the release of fiber entrapped charge after the fiber is deposited. In Figure 3 (a) and (c), an identical square wave patterned toolpath is designed for both experimental substrate samples (PS substrate as non-conductive, ITO coated glass substrate as conductive). Two aligned fibers are assigned to a group with set S_f = 200 μm within each group and set S_f = 2000 μm between groups. Figure 3 (b) displays measured S_f of grouped fibers on each substrate. The fibers on the non-conductive substrate yields a larger measured S_f compared with set S_f, as indicated by the solid red line. In contrast, the measured S_f on the conductive substrate is slightly smaller than the set S_f. The d_f is also plotted to show repeatability for the printed fiber diameter parameter. The Figure 3 (f) schematic demonstrates groups of paired fibers printed with their relative positions varying a function of the substrate conductivity.

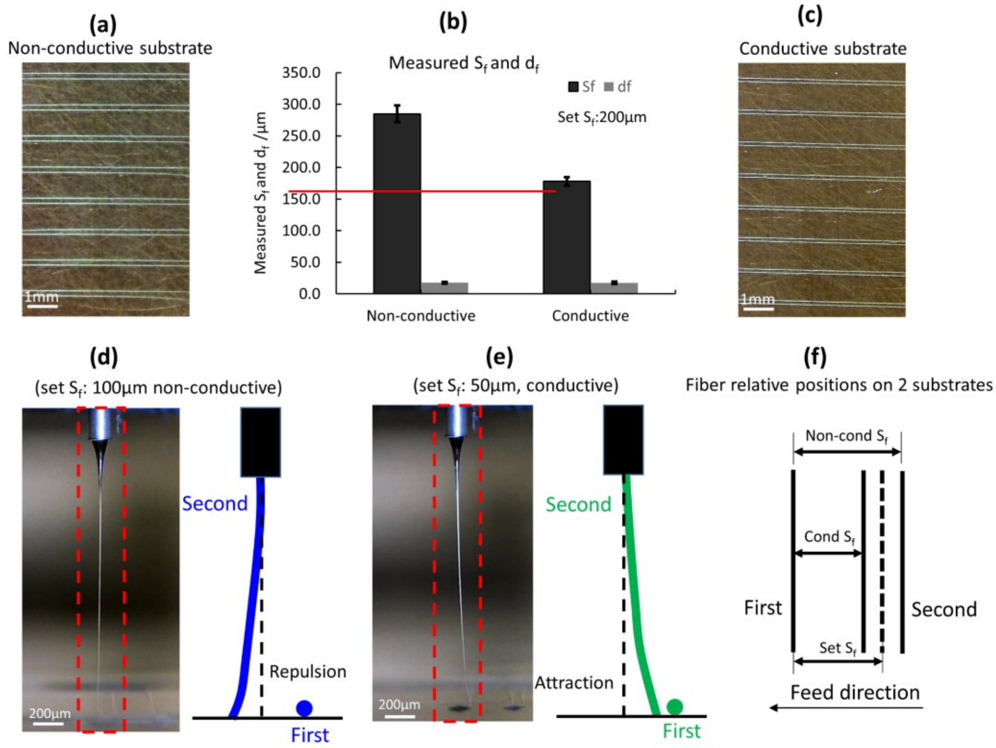

Figure 3. The effect of substrate conductivity on inter-fiber distance (S_f): **(a), (c)** The fibers deposited on non-conductive substrate and conductive substrate; **(b)** Measured S_f of the samples printed in **(a), (c); (d)-(e)** Attraction and repulsion phenomenon observed perpendicular to the print direction; **(f)** Schematic shows how two fibers are printed and possible relative positions.

The newly printed fiber tends to be attracted by the pre-existing fiber if the substrate is conductive, and repelled on a non-conductive substrate. This phenomenon is further verified by the captured images along the print direction in Figure 3 (d) and (e). For the two fibers shown in Figure 3 (f), the first fiber is vertically deposited at a designated position, the second fiber is deposited to the left of the first fiber at a set $S_f = 50$ µm. It is observed that the newly printed fiber is attracted and adheres to the preexisting fiber, where the fiber jet is deflected sideways in the direction perpendicular to the print direction. On the other hand, when the two fibers are deposited onto a non-conductive substrate, repulsion exerted on the newly printed fiber is observed, deflecting the jet away from the preexisting fiber. This phenomenon demonstrates the differential effects of substrate conductivity on the measured S_f compared to the set S_f at smaller set S_f regimes.

3.3. Relationship between set S_f and measured S_f on variable substrate conductivities

In this section, the aim is to understand the relationship between measured S_f and set S_f on substrates with divergent conductive properties. For visualization, Figure 4(a) shows

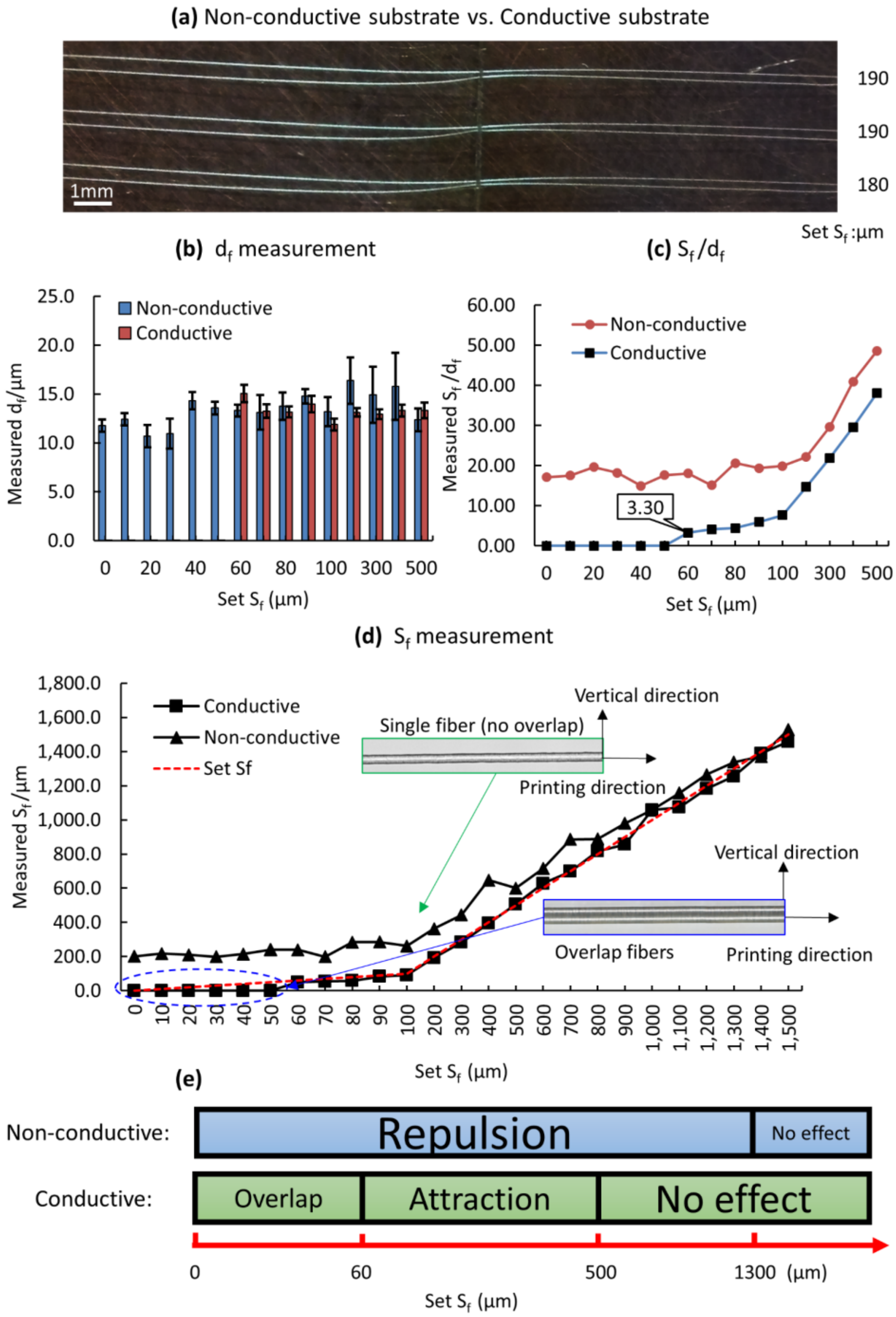

Figure 4. Relationship between set S_f and measured S_f on substrate with different conductivities; **(a)** The printed fibers on two aligned substrates where the left is non-conductive, and the right is conductive; **(b)** Measurement of d_f as a function of set S_f on two substrates; **(c)** The ratio of measured S_f over measured d_f ; **(d)** Measured S_f as a function of set S_f on two substrates, where measured S_f is larger than set S_f on the non-conductive substrate, and measured S_f is smaller than set S_f on the conductive substrate. When the set S_f is lower than 60 µm, the two fibers on the conductive substrate exhibit overlap; **(e)** Scale bar shows charge interaction between two fibers.

printed fibers on two aligned substrates, where the measured S_f on a non-conductive substrate is larger than that on a conductive substrate. For quantitative analysis, several groups of fibers with set S_f from 0-1500 μm are printed on the two substrate types. Specifically, the interval is 10 μm when set S_f is prescribed for the 0-100 μm range while the interval is 100 μm for the 100-1500 μm range. Furthermore, Figure 4(b) shows the plot of the fiber diameter d_f for all samples ranging from 10.7 μm to 16.38 μm with an average $d_f = 13.39 \pm 1.38$ μm, thereby indicating stability of the measured fiber diameter parameter during printing. The measured S_f/d_f as a function of set S_f is plotted in Figure 4(c). This ratio is considered as a critical indicator to evaluate how closely the adjacent fibers can approach each other. It is noted that the smallest S_f/d_f achieved is 3.30 on the conductive substrate. Since the d_f parameter is stable, the measured S_f is plotted in Figure 4(d) as a decoupled parameter to evaluate the fiber-fiber interaction caused by residual charge. The trend of measured S_f as a function of set S_f on the two substrates reveal an imbalance of forces exerted on the deposited fibers attributable to the substrate conductivity. In Figure 4(d), the measured S_f on the non-conductive substrate is consistently observed to be larger than the set S_f until set $S_f > 1300$μm. A decrement in the parametric difference (i.e. measured S_f – set S_f) is observed as the set S_f increases since the square trend line denoting the measured S_f approaches the red dashed line denoting the set S_f. On the other hand, the measured S_f on the conductive substrate approximates set S_f when the set S_f is above 500 μm, smaller when the set S_f is between 60-500 μm, and equals to 0 (i.e fiber overlap) when the set S_f is smaller than 60 μm, (circled in Figure 4 (d)). This indicates that an attractive resultant force on a second fiber becomes stronger as set S_f decreases. It is worth noting that, when the two fibers overlap, the fibers are aligned vertically in the layering direction (see image aside from the Figure 4 (d)).

3.4. Qualitative anaylsis of fiber attraction and repulsion phenomenon.

Although an observable attraction and repulsion phenomenon is studied in the previous sections, the reported mechanism of electric charges effects on aligned straight fibers is still rudimentary. Therefore, a mathematical model of electrostatic interaction between two fibers is proposed herein based on measured S_f data and a plot of the degree of offset (D_o) metric, which is defined as:

$$D_o = \frac{S_{f_{measured}} - S_{f_{set}}}{S_{f_{set}}} \quad (1)$$

The parameter D_o shown in Figure 5 (a) is indicated to correlate with the resultant force exerted on the second 'in-flight' fiber during deposition. Figure 5(b) shows the schematic illustrating the disposition for two printed adjacent fibers. To investigate the inter-fiber interaction in the lateral extent, an isometric view along the print direction (enlarged in Figure 5 (b)) provides the relative positions of two fibers. The second 'in-flight' fiber undergoes bending while approaching the substrate, where the angle (α in Figure 5(b)) formed between the tangent line at any position on the second fiber and a line parallel to the print direction ranges from 0° to 90°. It is assumed that there exists a segment of the second fiber that is strongly affected by inter-fiber interaction (red region labeled as ROI (region of interest) in Figure 5(b), which is a short fiber segment). Specifically, the red ROI of the second fiber is considered to interact with the first fiber. Furthermore, the upstream segment of the second fiber is deposited on the substrate and no longer assumed to be displaced by electrostatic forces (green region labeled as 'on substrate'). Figure5 (c) shows the simplified model, where the first fiber is considered as two line charges and the second fiber ROI as a two point charges, both of which carry a polarized charge distribution in the cross-sectional plane as shown in Figure 5(d-e). Here, the first fiber is polarized due to redistribution of charge carriers, yielding a negatively charged top section and a positively charged bottom section. The second 'in-flight' fiber carries a positively charged bottom section and a negatively charged upper section (or virtually so) while approaching the substrate. The charge

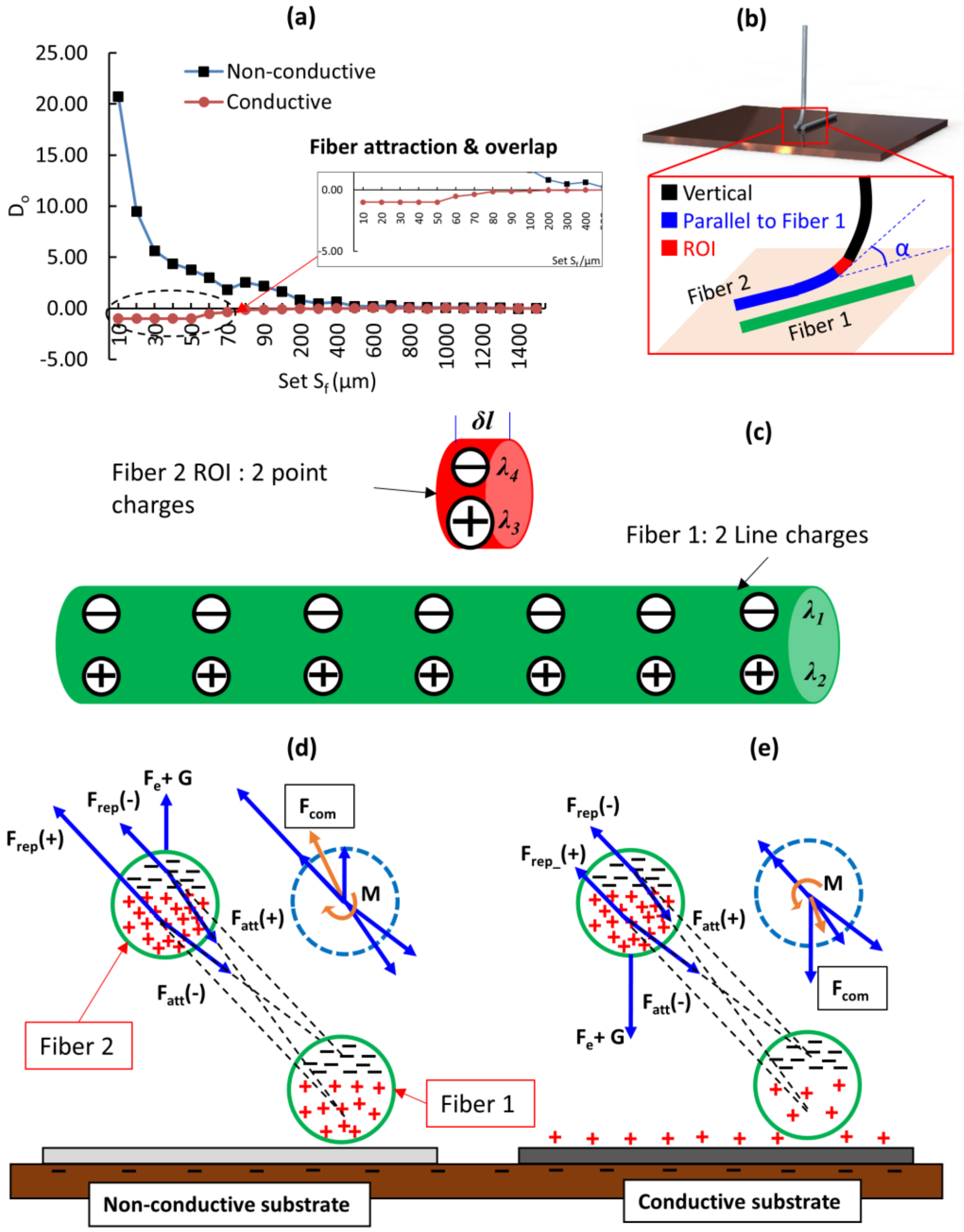

Figure 5. Model of electrostatic interaction between two fibers **(a)** The plot of degree of offset (D_o), proportional to the resultant force; **(b)** Schematic of fiber deposition shows the different segments of the second fiber where the red region is analyzed as an effective fiber segment which subjected to inter-fiber interaction; **(c)** Schematic shows the second fiber is simplified as two point charges and first fiber as two line charges;**(d)-(e)** The charge distribution of cross-sectional plane shows how substrate conductivity alters the repulsion and attraction phenomenon between two aligned fibers.

distribution on both substrates is indicated in Figure 5(d) and (e). Therefore, electrostatic forces exerted on the second fiber ROI is denoted in blue vectors. The resultant force $\boldsymbol{F}_{com}$ is also represented where the repulsion and attraction effects occur on the non-conductive conductive substrates, respectively.

Based on the simplifications of the ROI and charge distribution within fibers, the proposed simplified model is a system of two point charges (representing red ROI) and two infinitely long and uniform line charges (first fiber), where the charge densities for the cross-sectional plane are denoted by λ_1, λ_2, λ_3 and λ_4 (unit: C/m, shown in Figure 5(c)) that do not necessarily have the same magnitude. The electric field strength generated by an infinitely long and uniform line charge at a certain point A is expressed as:

$$\vec{\boldsymbol{E}} = 2k_e\lambda_i\vec{\boldsymbol{r}} \qquad (2)$$

where the k_e is the Coulomb constant ($k_e = 1/(4\pi\epsilon_0)$), and $\vec{r}$ is the vector starting at the point on the line charge nearest to A and terminating at A. Then the forces exerted on red ROI fiber segment (as two point charges) by the two line charges (deposited fiber with polarized charge distribution) with differential length δl can be written as:

$$\vec{\boldsymbol{F}}_{ij} = 2k_e\frac{\lambda_i\lambda_j\delta l}{r_{ij}}\hat{\boldsymbol{r}}_{ij}, i = 1,2, j = 3,4 \ (3)$$

where and $\hat{\boldsymbol{r}}_{ij}$ denotes the unit vector in the direction of the vector starting at the point on line charge i nearest to the point charges j terminating at point charge $\lambda_j\ \delta l$, , i = 1,2, j = 3,4. Also, the force exerted on the red ROI by external electric field notwithstanding the inter-fiber interaction is given as:

$$\vec{\boldsymbol{F}}_e = (\lambda_3 - \lambda_4)\boldsymbol{E_l} \ (4)$$

where $\boldsymbol{E_l}$ represents the local electrostatic field strength as a result of the interaction between the high voltage nozzle tip, collector, and the substrate. Thus, the resultant force exerted on ROI can be represented as:

$$\vec{\boldsymbol{F}}_{com} = \sum_{i=1}^{2}\sum_{j=3}^{4}\vec{\boldsymbol{F}}_{ij} + \vec{\boldsymbol{F}}_e + \vec{\boldsymbol{G}} \quad (5)$$

where $\vec{\boldsymbol{G}}$ is the gravity. The direction of resultant force is affected by the relative values of λ_1, λ_2, λ_3, and λ_4 as well as $\boldsymbol{E_l}$. In this model, the conductivity of the substrate plays a critical role in altering the magnitude and direction of $\boldsymbol{E_l}$, along with the charge distribution of the two point charges and the charge density of the two line charges. Thus, the final effect can be either attractive or repulsive as a function of the substrate properties. The mechanism that supports this hypothesis is that the extent to which the excess positive charges entrapped within the fiber is transferred to the ground collector is determined by substrate conductivity, and in turn affecting the fiber interaction.

The substrate conductivities (or resistivity) and set S_f are two variables in this model, whose effect on inter-fiber attraction/repulsion can be further discussed for two specific cases.

Case 1: Fiber repulsion/interaction as a function of substrate conductivity.

Empirically, the fiber deposited retains a certain amount of negative charge which cannot be transferred to the ground or substrates. Based on this, the charge density of second fiber ROI and first fiber are:

$$\lambda_1 = -\lambda, \lambda_2 = k_\rho \lambda, q_3 = e_c \lambda, q_4 = -\lambda, (k_\rho, e_c \in R^+)$$

where λ represents absolute value of negative charge density in the upper part of both fibers. The denoted k_ρ is the charge transport coefficient representing the capability of positive charge transport between fiber and substrate by way of contact, and e_c (≥1) is the charge emission coefficient representing the capability of two mechanisms that inject charge carriers into a viscous polymer, namely electrical-field induced emission and the induced charge dissociation [7]. The forces exerted on the second fiber from the pre-existing first fiber along the line direction (i.e. formed by the two centers of the fiber cross-sectional planes) can be written as:

$$\vec{\boldsymbol{F}}_f = \sum_{i=1}^{2}\sum_{j=3}^{4}\vec{\boldsymbol{F}}_{ij} = 2k_e\delta l\left(\frac{\lambda^2}{r_{14}}\hat{\boldsymbol{r}}_{14} + \frac{k_\rho e_c \lambda^2}{r_{23}}\hat{\boldsymbol{r}}_{23} - \frac{k_\rho \lambda^2}{r_{24}}\hat{\boldsymbol{r}}_{24} - \frac{e_c \lambda^2}{r_{13}}\hat{\boldsymbol{r}}_{13}\right) \quad (6)$$

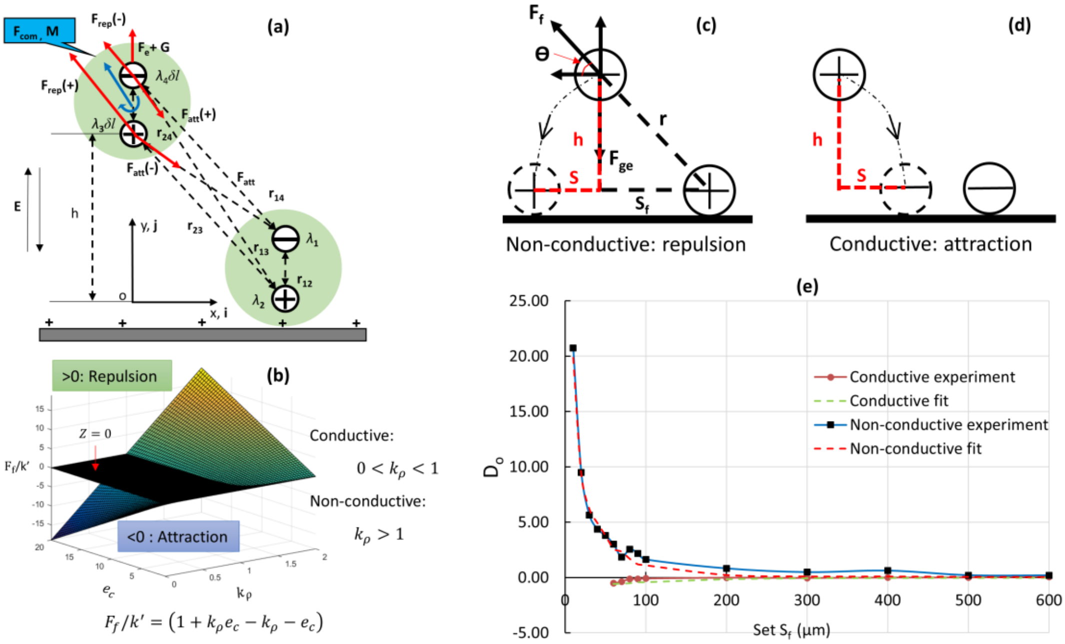

Figure 6. **(a)** Schematic of electrostatic interactions between line-point charge in a static electric field; **(b)** The 3D force plane exerted on the second fiber as a function of e_c and k_ρ; **(c)-(d)** Model of force D_o and S_f on the non-conductive and conductive substrates; **(e)** The plot of fitted model (Equation (11)) and experimental data of D_o as a function of S_f.

Since the distance between λ_1, λ_2 (as well as λ_3, λ_4) is negligible compared to the distance between λ_1, λ_4 (as well as λ_2, λ_3), therefore $r_{ij} \cong r, i = 1,2, j = 3,4$. The magnitude of $\vec{\boldsymbol{F}}_f$ can be denoted as:

$$F_f = k'(1 + k_\rho e_c - k_\rho - e_c) \quad (7)$$

where $k' = 2k_e \delta l \lambda^2 / r^2$. Based on Equation (7), the force along the line (formed by the two centers of the fiber cross-sectional planes) is correlated to k_ρ and e_c. The relative force plane (F_f/k') as a function of the two parameters is plotted in Figure 6(b). When printing on the conductive substrate, $0 < k_\rho < 1$, $F_f/k' < 0$, representing attraction. When printing on the non-conductive substrate, $k_\rho > 1$, $F_f/k' > 0$, representing repulsion.

Case 2: Fiber repulsion/interaction as a function of set S_f.

As set S_f changes, F_f varies. D_o is positively related to F_f based on the model. By letting F_{ge} represent the magnitude of $\vec{\boldsymbol{F}}_e + \vec{\boldsymbol{G}}$, the fiber segment is assumed to be stationary in the cross-sectional plane. As S_f changes, the distance between the fibers changes. According to Figure 6 (c), Equation (7) can be re-written as:

$$F_f = \frac{k_{e_c\rho}}{r} \quad (8)$$

where

$$k_{e_c\rho} = 2k_e\delta l\left(1 + k_\rho e_c - k_\rho - e_c\right)\lambda^2 \quad (9)$$

Two assumptions are made to determine the relationship between D_o and S_f:

(1) The first fiber is stretched by the translational stage and becomes parallel to the previously deposited fiber at an initial height of h_0, with a velocity of v_h ($0<v_h<v_c$), (v_c represents the critical translational stage speed, measured to be ~0.02m/s in the experiments) where the fiber interaction starts.

(2) After the fiber segment (ROI) is falls below h_0, the charge within the fiber redistribute and the ROI is subjected to electrostatic forces from the first fiber, where the following non-linear ordinary differential equation system can be derived:

$$\begin{cases} \delta m \dfrac{d^2 S}{dt^2} = F_h = F_f cos\theta \\ \delta m \dfrac{d^2 H}{dt^2} = F_v = -F_{ge} + F_f sin\theta \end{cases} \quad (10)$$

where δm is the mass of the prescribed ROI fiber segment. Substitution of equation (8) into (10) yields:

$$\begin{cases} \delta m \dfrac{d^2 S}{dt^2} = \dfrac{k_{e_c\rho}\,(S + S_f)}{\sqrt{\left(\left(S + S_f\right)^2 + h^2\right)}} \\ \delta m \dfrac{d^2 h}{dt^2} = F_{ge} - \dfrac{k_{e_c\rho}\,h}{\sqrt{\left(\left(S + S_f\right)^2 + h^2\right)}} \end{cases} \quad (11)$$

where h denotes the vertical distance between ROI and substrate. Letting S denote the horizontal distance that the ROI travels, the initial conditions can be obtained as:

$$\begin{cases} h(0) = h_0, h'(0) = v_0 \\ S(0) = 0, S'(0) = 0 \end{cases} \quad (12)$$

In addition to the independent variable time (t), and dependent variables (S, h), the unknown parameters are [h_0, v_0, k_{mew}, g_e], where the h_0 is the height that inter-fiber interaction occurs, at when the fiber has a vertical speed of v_0. Based on the experimental configuration, $0 < v_0 < 0.02$ m/s, $0 < h_0 < 0.012$ m. The generalized coefficient called MEW coefficient is denoted by $k_{mew} = k_{e_c\rho} / \delta m$ and $g_e = F_{ge} / \delta m$, represents the acceleration caused by gravity and electric field. S_f and D_o are experimental data applied to fit the $S(t)$ and $h(t)$. By using Matlab (ode45 solver) to solve the ordinary differential equation system with properly tuning the unknown parameters by grid search method, a parameter set of the line-point charge model fit of the experimental data in Figure 5(a) is derived, which is shown in Table 2. The fitted results provide an approximate range of unknown parameters, which is not necessarily the actual data due to small sample size of experimental data.

Table 2. The fitted parameters in Equations (11) and (12).

Fitted parameters	Vertical height: h_0 (μm)	Vertical speed v_0 (m/s)	MEW coefficient: k_{mew}(N)	Gravitational and electric field acceleration: g_e (N/m^2)
non−conductive	~110	~0.0008	10^{-5}	0.1
conductive	~90	~0.00014	-10^{-6}	0.01

3.5 Model verification by measuring residual charge using Faraday cup

Based on the model proposed in the previous section, the residual net charge entrapped within the aligned fibers is negative and positive on the conductive and non-conductive substrates, respectively. Therefore, within a range of prescribed layer thickness, the fabricated layered structures, termed scaffolds herein, should assume a negative charged on the conductive substrate, and a net positive charge on the non-conductive substrate. To verify this model, two 15-layer scaffolds with dimensions of 10×50 mm are printed on two different

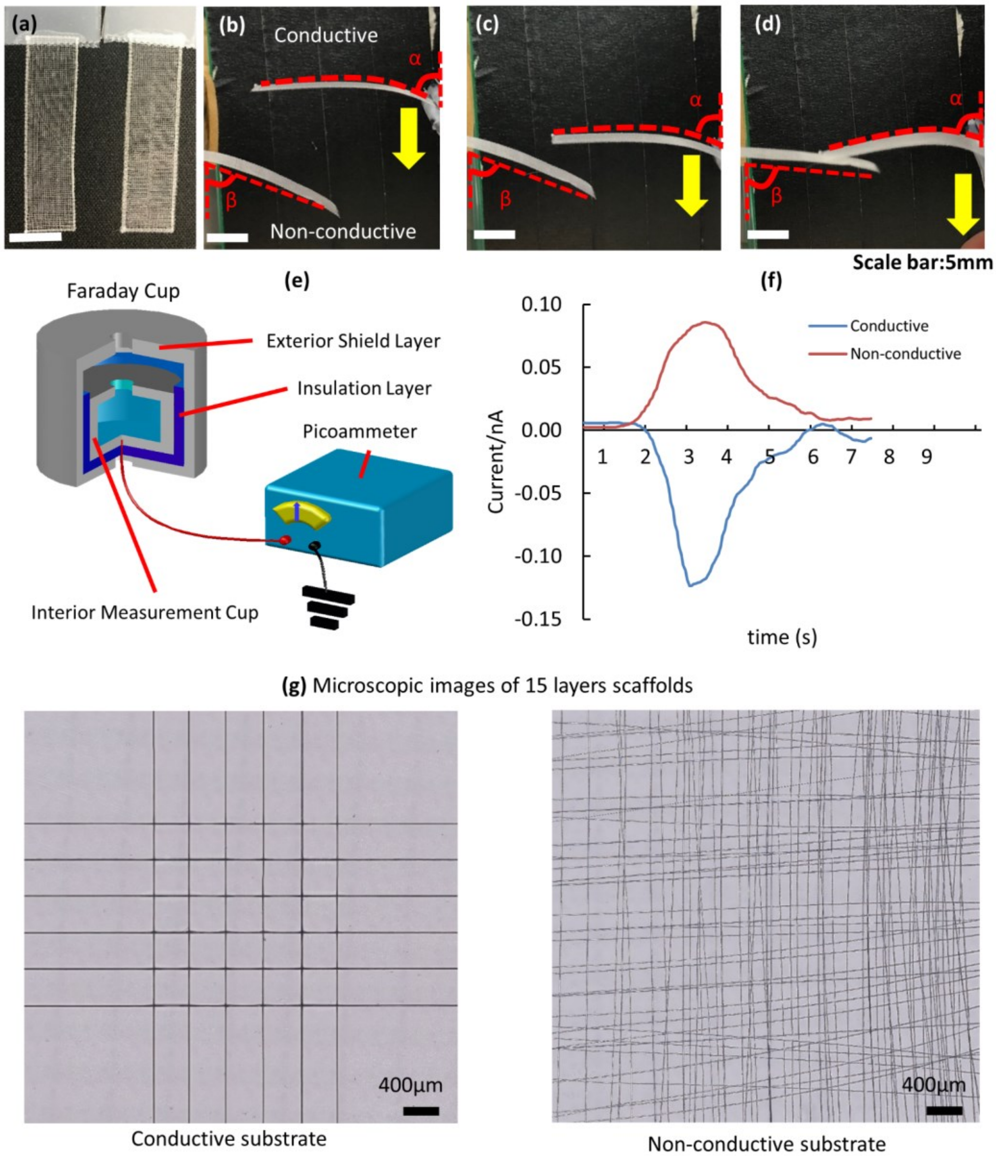

Figure 7. Verification of the line-point charge fiber interaction model: **(a)** Two printed scaffolds, the left is on conductive substrate, right on non-conductive substrate; **(b)-(d)** The three images show that when the two scaffolds approach one another, attraction is observed; **(e)** Schematic of a Faraday cup for a residual charge measurement; **(f)** Charge measurement of two scaffolds in (a); **(g)** 15 layers of scaffolds in both substrates.

substrates as shown in Figure 7(a). The scaffolds are then gently removed from the substrate with insulating tweezers, which is verified in advance to be neutral by a customized Faraday cup design as shown in Figure 7(e). First, when the two scaffolds approach one another, an attraction phenomenon is observed (in Figure 7(b)-(d)), where both angles (α and β) measured between the one end of the scaffolds and a vertical mount increase. To further quantify the amount of net charge for the two scaffolds, the Faraday cup measurement is carried out. Upon insertion of the two scaffolds into the Faraday cup, the net charge on the scaffold for the conductive and non-conductive substrates is determined to be negative and positive, respectively. In addition, microscopic images of 15-layered scaffolds on the two substrates are shown in Figure 7(g), indicating that the fibers align vertically with precise overlap on the conductive substrate but randomly deposit on the non-conductive substrate. These results are consistent with the model proposed in the preceding section.

4. Discussion

As a current state-of-art AM technique, MEW enables the fabrication of micron or sub-micron scale engineered biological cell substrates. Although the essential role of fiber diameter is well-recognized [17,27], tight control over the inter-fiber distance parameter S_f and the underlying mechanism is still under development. In the context of observed fiber repulsion and attraction phenomena during the MEW process, systematic experiments and mathematical models are necessary to understand the charge mechanisms that dictate the printed fiber-based structural outcomes. By printing a series of aligned fibers on substrates with different conductivities and measuring current during the fiber printing process, insights into this phenomenon are reported herein.

First, fibers printed with an oscillating toolpath assume two distinct types of alignment patterns on substrates with different conductivities. When the substrate is conductive, fibers are strongly polarized by the local electric field whose positive charges will be largely transported to the substrate due to direct physical contact or inverse corona discharge. This results in the fiber's weak electric negativity but strong polarization accompanied by fiber overlap at small set S_f and attraction at large set S_f. When the substrate is non-conductive, fiber polarization is weakened due to the relatively weak local electric field and abundant positive charges retained in the fibers, both of which result in the inter-fiber repulsion and random deposition of the printed fibers. From the symmetric plot of the measured divergent fibers, it is noteworthy that the weakened electrical field on a non-conductive substrate confers a random and unbiased effect on the fiber positioning whereby the inter-fiber spacing between fibers can be primarily attributed to preexisting fibers.

Therefore, during the printing process on substrates with various conductivities, the repulsive and attractive forces are observable between (1) the second “in-flight” fiber and substrate (repulsion on non-conductive substrate, attraction on conductive substrate), (2) the second “in-flight” fiber and deposited fiber (repulsion on non-conductive substrate, attraction on conductive substrate), which compromise the accuracy of S_f. The type (1) instability is primarily caused by weak local electrical field near substrate, which can be compensated by selecting an appropriate critical translational stage speed. However, type (2) instability is primarily attributed to the fiber-fiber and fiber-substrate interaction. Systematically, by setting different S_f (0-1500 μm) on both substrates, the repulsion between fibers is strong enough to prevent fibers from overlapping on non-conductive substrate even with set $S_f = 0$ μm. However, the fiber overlaps the previous one once the set $S_f < 60$ μm (approximately, not exactly the same every time) when printing on conductive substrate. The trend line for D_o suggests that a line-point charge model can explain the repulsion and attraction phenomenon on two substrates. According to the line-point charge model, the substrate conductivity alters the local electrical field strength and charge amount on the substrate surface, and in turn the net charge amount and distribution in the fibers once in contact with the substrate. Therefore, the final resultant force can be either repulsive or attractive. The model explains why the fibers only overlap in vertical direction as well, where negative charge carriers are forced to distribute at the topmost region of the fiber, the final resultant force becomes vertical as the two fibers come into close apposition. Also, based on the model, the function between D_o and set S_f can be derived and fitted, where the ROI of newly deposited fiber is forced to move laterally at some height due to the existence of electrostatic forces. Furthermore, post-measurement of charge amount by using a Faraday cup verifies the model effectively.

5. Conclusions

In this paper, experimental studies are conducted to investigate the charge effect on fiber alignment accuracy. The relationship between electrostatic forces and the repulsive-attractive phenomenon has been revealed and modeled. The advanced mathematical model explains the repulsion and attraction interaction, as well as the fiber-overlapping phenomenon. In the two cases of analyses of the model, as set S_f or substrate conductivity changes, the resultant force exerted on the second newly deposited fibers is altered. Based on the experimental results, the charge transport path during the fiber printing process can be revealed: (1) Pathway. The positively charged fiber (or material droplets) transfers charge carriers to the substrates. A conductive substrate has superior conductivity to allow charge transport to the ground/substrate surface compared to a non-conductive substrate. (3) Residual. More positive charges remain in the deposited fibers on the non-conductive substrate than those on the conductive substrate, as evidenced by the repulsion phenomenon between fibers on a non-conductive substrate and attraction on a conductive substrate.

Once the underlying mechanism is well-understood, charge removal strategies can be proposed to exert precision control over the fiber print structural outcomes. For example, a heat-based charge removal method may be applied, where the entrapped charge within the fiber may be radially transported to the fiber surface as the process temperature increases. Another potential method is to use an electrolytic substrate, such as a hydrogel material to allow the charge carriers to be neutralized upon deposition. However, the specific scope of this paper is to investigate charge effects during the MEW process. Additional quantitative variations in the substrate conductivities would need to be tested to confirm the overall trend of the resultant force exerted on the newly deposited fibers. The relationship between the charge amount and the scaffold layer-height is another key consideration for large-scale fabrication of ordered three-dimensional scaffolds. Finally, a refined mathematical model is essential to identify the fundamental physics of charge transport inherent to the MEW process.

Acknowledgments: The work presented in this paper was supported by the National Science Foundation under Award No. CMMI-MME-1663095. Any opinions, findings and conclusions or recommendations expressed in this publication are those of the authors and do not necessarily reflect the views of the National Science Foundation.

Conflicts of Interest: The authors declare no conflict of interest.

Data Availability: The raw/processed data required to reproduce these findings cannot be shared at this time as the data also forms part of an ongoing study.

References

[1] D.B. Kolesky, K.A. Homan, M.A. Skylar-Scott, J.A. Lewis, Three-dimensional bioprinting of thick vascularized tissues, Proc. Natl. Acad. Sci. . 113 (2016) 3179–3184. http://www.pnas.org/content/113/12/3179.abstract.

[2] G. Hochleitner, T. Jüngst, T.D. Brown, K. Hahn, C. Moseke, F. Jakob, P.D. Dalton, J. Groll, Additive manufacturing of scaffolds with sub-micron filaments via melt electrospinning writing, Biofabrication. 7 (2015). doi:10.1088/1758-5090/7/3/035002.

[3] Current status of three-dimensional printing inks for soft tissue regeneration, Tissue Eng. Regen. Med. 13 (2016) 636. http://dx.doi.org/10.1007/s13770-016-0125-8.

[4] H. Ding, R.C. Chang, Simulating image-guided in situ bioprinting of a skin graft onto a phantom burn wound bed, Addit. Manuf. 22 (2018). doi:10.1016/j.addma.2018.06.022.

[5] D.A. Saville, Electrohydrodynamics :The Taylor-Melcher Leaky Dielectric Model, Annu. Rev. Fluid Mech. 29 (1997) 27–64. doi:10.1146/annurev.fluid.29.1.27.

[6] F. Tourlomousis, H. Ding, D.M. Kalyon, R.C. Chang, Melt electrospinning writing process guided by a "Printability Number," J. Manuf. Sci. Eng. Trans. ASME. 139 (2017). doi:10.1115/1.4036348.

[7] F.M. Wunner, M. Wille, T.G. Noonan, O. Bas, P.D. Dalton, E.M. De-juan-pardo, D.W. Hutmacher, Melt Electrospinning Writing of Highly Ordered Large Volume Scaffold Architectures, 1706570 (2018) 1–6. doi:10.1002/adma.201706570.

[8] T.D. Brown, P.D. Dalton, D.W. Hutmacher, Melt electrospinning today: An opportune time for an emerging polymer process, Prog. Polym. Sci. 56 (2016) 116–166. doi:https://doi.org/10.1016/j.progpolymsci.2016.01.001.

[9] P. Luana, C. Andrea, T. Cagri, P. Dario, Industrial Upscaling of Electrospinning and Applications of Polymer Nanofibers: A Review, Macromol. Mater. Eng. 298 (2013) 504–520. doi:10.1002/mame.201200290.

[10] J. Ko, N.K. Mohtaram, F. Ahmed, A. Montgomery, M. Carlson, P.C.D. Lee, S.M. Willerth, M.B.G. Jun, Fabrication of poly (ϵ-caprolactone) microfiber scaffolds with varying topography and mechanical properties for stem cell-based tissue engineering applications, J. Biomater. Sci. Polym. Ed. 25 (2014) 1–17. doi:10.1080/09205063.2013.830913.

[11] Q.P. Pham, U. Sharma, A.G. Mikos, Electrospinning of Polymeric Nanofibers for Tissue Engineering Applications: A Review, Tissue Eng. 12 (2006) 1197–1211. doi:10.1089/ten.2006.12.1197.

[12] P.D. Dalton, C. Vaquette, B.L. Farrugia, T.R. Dargaville, T.D. Brown, D.W. Hutmacher, Electrospinning and additive manufacturing: converging technologies, Biomater. Sci. 1 (2013) 171–185. doi:10.1039/C2BM00039C.

[13] Y. Wu, B. Wu, S. Vijayavenkataraman, Y.S. Wong, J.Y.H. Fuh, Crimped fiber with controllable patterns fabricated via electrohydrodynamic jet printing, Mater. Des. 131 (2017) 384–393. doi:https://doi.org/10.1016/j.matdes.2017.06.027.

[14] F. Tourlomousis, A. Babakhanov, H. Ding, R.C. Chang, A novel melt electrospinning system for studying cell substrate interactions, in: ASME 2015 Int. Manuf. Sci. Eng. Conf. MSEC 2015, 2015. doi:10.1115/MSEC20159443.

[15] E. McColl, J. Groll, T. Jungst, P.D. Dalton, Design and fabrication of melt electrowritten tubes using intuitive software, Mater. Des. 155 (2018) 46–58. doi:https://doi.org/10.1016/j.matdes.2018.05.036.

[16] Modeling 3D melt electrospinning writing by response surface methodology, Mater. Des. (2018). http://dx.doi.org/10.1016/j.matdes.2018.03.053.

[17] T.D. Brown, F. Edin, N. Detta, A.D. Skelton, D.W. Hutmacher, P.D. Dalton, Melt electrospinning of poly(ε-caprolactone) scaffolds: Phenomenological observations associated with collection and direct writing, Mater. Sci. Eng. C. 45 (2014) 698–708. doi:https://doi.org/10.1016/j.msec.2014.07.034.

[18] G. Collins, J. Federici, Y. Imura, L.H. Catalani, Charge generation, charge transport, and residual charge in the electrospinning of polymers: A review of issues and complications, J. Appl. Phys. 111 (2012) 44701. doi:10.1063/1.3682464.

[19] L.H. Catalani, G. Collins, M. Jaffe, Evidence for Molecular Orientation and Residual Charge in the Electrospinning of Poly(butylene terephthalate) Nanofibers, Macromolecules. 40 (2007) 1693–1697. doi:10.1021/ma061342d.

[20] D.H. Reneker, A.L. Yarin, H. Fong, S. Koombhongse, Bending instability of electrically charged liquid jets of polymer solutions in electrospinning, J. Appl. Phys. 87 (2000) 4531–4547. doi:10.1063/1.373532.

[21] J. van Turnhout, Thermally Stimulated Discharge of Polymer Electrets, Polym. J. 2 (1971) 173. http://dx.doi.org/10.1295/polymj.2.173.

[22] A.L. Yarin, S. Koombhongse, D.H. Reneker, Bending instability in electrospinning of nanofibers, J. Appl. Phys. 89 (2001) 3018–3026. doi:10.1063/1.1333035.
[23] M.M. Hohman, M. Shin, G. Rutledge, M.P. Brenner, Electrospinning and electrically forced jets. I. Stability theory, Phys. Fluids. 13 (2001) 2201–2220. doi:10.1063/1.1383791.
[24] Y.M. Shin, M.M. Hohman, M.P. Brenner, G.C. Rutledge, Experimental characterization of electrospinning: the electrically forced jet and instabilities, Polymer (Guildf). 42 (2001) 9955–9967. doi:https://doi.org/10.1016/S0032-3861(01)00540-7.
[25] J.H. and P.X. and D. Li, Development of melt electrohydrodynamic 3D printing for complex microscale poly (ε -caprolactone) scaffolds, Biofabrication. 8 (2016) 35008. http://stacks.iop.org/1758-5090/8/i=3/a=035008.
[26] A.Y. and S.J.H. and P.D. Dalton, Additive manufacturing of polymer melts for implantable medical devices and scaffolds, Biofabrication. 9 (2017) 12002. http://stacks.iop.org/1758-5090/9/i=1/a=012002.
[27] B.T. D., D.P. D., H.D. W., Direct Writing By Way of Melt Electrospinning, Adv. Mater. 23 (2011) 5651–5657. doi:10.1002/adma.201103482.